Title

Optimizing detection and deep learning-based classification of pathological high-frequency oscillations in epilepsy.

Authors

Monsoor, Tonmoy
Zhang, Yipeng
Daida, Atsuro
et al.

Publication Date

2023-10-01

DOI

10.1016/j.clinph.2023.07.012

Peer reviewed

HHS Public Access

Author manuscript

Clin Neurophysiol. Author manuscript; available in PMC 2024 February 12.

Published in final edited form as:

Clin Neurophysiol. 2023 October ; 154: 129–140. doi:10.1016/j.clinph.2023.07.012.

Optimizing Detection and Deep Learning-based Classification of Pathological High-Frequency Oscillations in Epilepsy

Tonmoy Monsoor, MS[1], **Yipeng Zhang, MS**[1], **Atsuro Daida, MD, PhD**[2], **Shingo Oana, MD, PhD**[2], **Qiujing Lu, PhD**[1], **Shaun A. Hussain, MD, MS**[2], **Aria Fallah, MD, MS**[3], **Raman Sankar, MD, PhD**[2,4], **Richard J. Staba, PhD**[5], **William Speier, PhD**[6,7], **Vwani Roychowdhury, PhD**[1], **Hiroki Nariai, MD, PhD, MS**[2,4,*]

[1]Department of Electrical and Computer Engineering, University of California, Los Angeles, CA, USA

[2]Division of Pediatric Neurology, Department of Pediatrics, UCLA Mattel Children's Hospital, David Geffen School of Medicine, Los Angeles, CA, USA

[3]Department of Neurosurgery, UCLA Medical Center, David Geffen School of Medicine, Los Angeles, CA, USA

[4]The UCLA Children's Discovery and Innovation Institute, Los Angeles, CA, USA

[5]Department of Neurology, UCLA Medical Center, David Geffen School of Medicine, Los Angeles, CA, USA

[6]Department of Bioengineering, University of California, Los Angeles, CA, USA

[7]Department of Radiological Sciences, University of California, Los Angeles, CA, USA

Abstract

Objective: This study aimed to explore sensitive detection methods for pathological high-frequency oscillations (HFOs) to improve seizure outcomes in epilepsy surgery.

Methods: We analyzed interictal HFOs (80-500 Hz) in 15 children with medication-resistant focal epilepsy who underwent chronic intracranial electroencephalogram via subdural grids. The HFOs were assessed using the short-term energy (STE) and Montreal Neurological Institute (MNI) detectors and examined for spike association and time-frequency plot characteristics. A deep learning (DL)-based classification was applied to purify pathological HFOs. Postoperative seizure outcomes were correlated with HFO-resection ratios to determine the optimal HFO detection method.

Results: The MNI detector identified a higher percentage of pathological HFOs than the STE detector, but some pathological HFOs were detected only by the STE detector. HFOs detected by both detectors had the highest spike association rate. The Union detector, which detects HFOs identified by either the MNI or STE detector, outperformed other detectors in predicting postoperative seizure outcomes using HFO-resection ratios before and after DL-based purification.

[*]Corresponding author: Hiroki Nariai, MD, PhD, MS, Division of Pediatric Neurology, Department of Pediatrics, UCLA Mattel Children's Hospital, David Geffen School of Medicine, Los Angeles, CA, USA, Address: 10833 Le Conte Ave, Room 22-474, Los Angeles, CA 90095-1752, USA, hnariai@mednet.ucla.edu.

Conclusions: HFOs detected by standard automated detectors displayed different signal and morphological characteristics. DL-based classification effectively purified pathological HFOs.

Significance: Enhancing the detection and classification methods of HFOs will improve their utility in predicting postoperative seizure outcomes.

Keywords

HFO; STE; MNI; machine learning; deep learning

1. INTRODUCTION:

Complete resection of the epileptogenic zone (EZ: areas of the brain responsible for generating seizures) is necessary to achieve freedom from seizures in drug-resistant focal epilepsy (Rosenow et al. 2001). Discovering a biomarker that can accurately map the spatial extent of EZ will be significant. Research on epilepsy, involving both humans and animals, has proposed that intracranially recorded interictal high-frequency oscillations (HFOs) on EEG is a promising spatial neurophysiological biomarker of EZ (Bragin et al. 1999a; Bragin et al. 1999b; Worrell et al. 2008; Zijlmans et al. 2009). There have been many studies in the past showing the correlation between postoperative seizure freedom and the resection of brain regions generating HFOs. (Jacobs et al. 2010; Wu et al. 2010; Akiyama et al. 2011; Nariai et al. 2011; van 't Klooster et al. 2015). However, a recent multi-institutional prospective study was unable to reproduce the findings (Jacobs et al. 2018), and a clinical trial that was recently published could not demonstrate that HFO-guided resection during electrocorticography (ECoG) resulted in better seizure outcomes than standard spike-guided resection (Zweiphenning et al. 2022).

At this stage, although HFOs show promise, it is unclear whether it can be used to guide epilepsy surgery. Some technical issues with HFO analysis include the following: (1) The standard detection methods of HFOs have not been established (Remakanthakurup Sindhu et al. 2020; Wong et al. 2021). Currently, there are various methods available for HFO detection, including the STE (Staba et al. 2002), Short Line Length (SLL) (Gardner et al. 2007), and Hilbert transform (Crepon et al. 2010) methodologies. The recent and widely used method is the MNI detector (Zelmann et al. 2009), in which the HFO detection incorporates information from previously detected baselines to simulate expert HFO analysis to enhance its detection sensitivity. However, although the STE detector is simple and commonly used, it is still unclear whether this simpler method is less effective in detecting HFOs than the more sophisticated MNI detector. (2) The presence of physiological HFOs complicates the interpretation of the results (Frauscher et al. 2017; Frauscher et al. 2018). Currently, no methods are available to detect pathological HFOs, while rejecting physiological HFOs and artifacts. Visual analysis by a human expert is commonly performed, but it is time-consuming and has limitations in inter-rater reliability (Spring et al. 2017; Nariai et al. 2018). Although it works well for artifact rejection, human experts cannot confidently annotate each event as pathological or physiological except for recognizing HFOs with or without spikes. Efforts to selectively detect pathological HFOs have been attempted, including automated detection of spikes along with HFOs (Weiss et al. 2016; Guth et al. 2021) and cross-frequency coupling analysis (Nonoda et al. 2016; Motoi

et al. 2019; Kuroda et al. 2021). However, the evidence of its efficacy in differentiating pathological and physiological HFOs is still limited. Furthermore, it remains uncertain whether the MNI detector is more sensitive than the simple STE-based detection in detecting pathological HFOs.

In recent work, we developed a novel weakly-supervised DL algorithm, using channel resection status as DL labels, to characterize the pathological HFOs generated by EZ (Zhang et al. 2022b). In another related work, we utilized a similar framework, with functional cortical mapping results as DL labels, to characterize the physiological HFOs generated by the eloquent cortex (EC) (Zhang et al. 2022a). However, we applied the DL-based classifiers after we detected HFOs using the STE detector. It is unknown whether we had increased sensitivity in detecting pathological or physiological HFOs before applying the classifiers with the MNI detector or a combination of both.

The present study aimed to provide insights into what HFO detection methods should be used to maximize the sensitivity of pathological HFOs by meticulously characterizing HFOs detected by the STE and MNI detectors. We also engineered the Union detector, which encompassed events detected by either STE or MNI detectors to further enhance the sensitivity of the detection. Then, the detected HFOs from each detector were evaluated for their association with spikes and time-frequency characteristics. Finally, our previously developed novel DL-based classifier was applied to determine what detection methods would provide the most sensitive detection of pathological HFOs, and what HFO detection method would provide the most accurate postoperative seizure outcomes.

2. METHODS:

2.1. Patient cohort

This study employed a retrospective cohort design. We consecutively recruited children (under the age of 21) who were suffering from medically refractory epilepsy—characterized by monthly or more frequent seizures and the inefficacy of more than three anti-seizure medications—from the Pediatric Epilepsy Program at UCLA. These children had intracranial electrodes implanted for epilepsy surgery planning and subsequent cortical resection between August 2016 and August 2018. Those who underwent a diagnostic stereo-EEG evaluation, which wasn't intended for resective surgery, were excluded from the study.

2.2. Standard protocol approvals, registrations, and patient consent

The UCLA's institutional review board approved the involvement of human subjects and dispensed with the necessity for written informed consent. All the tests were regarded as clinically relevant for patient care, and all the EEG data used in this retrospective study was anonymized before it was extracted and analyzed. This study was not classified as a clinical trial and was not registered in any public registry.

2.3. Patient evaluation

All children referred during the study period, who were suffering from medically refractory epilepsy, underwent a systematic pre-surgery evaluation. This included inpatient video-EEG

monitoring, high-resolution brain magnetic resonance imaging (MRI) of 3.0 Tesla, and 18 fluoro-deoxyglucose positron emission tomography (FDG-PET), coupled with MRI-PET co-registration. The boundaries and scope of the resections were primarily based on the seizure onset zone (SOZ), which is clinically identified as the areas initially showing continuous rhythmic waveforms at the beginning of typical seizures. In certain instances, to avoid causing unacceptable neurological damage, the seizure onset zones were not fully resected.

2.4. Subdural electrode placement

Surgical implantation was performed for macroelectrodes, which included platinum grid electrodes with an intercontact distance of 10 mm, and depth electrodes, made of platinum with a 5 mm intercontact distance. The total number of electrode contacts for each patient ranged from 40 to 128, with a median of 96 contacts. The positioning of these intracranial electrodes was primarily guided by the results of scalp video-EEG recording and neuroimaging studies. All electrode plates were sewn to neighboring plates, the dura mater's edge, or both, in order to minimize the movement of subdural electrodes post-placement.

2.5. Acquisition of three-dimensional (3D) brain surface images

We collected high-resolution 3D magnetization-prepared rapid acquisition with gradient echo (MPRAGE) T1-weighted images of the whole head preoperatively. Utilizing post-implant computed tomography (CT) images, we created a FreeSurfer-based 3D surface image with the locations of the electrodes directly identified on the brain surface (Zhang et al. 2022b). Furthermore, digital photographs were captured intraoperatively before the dura was closed to improve the spatial precision of electrode placement on the 3D brain surface. When the area was re-exposed for resective surgery, we visually verified that the electrodes had remained in place, matching the digital photo taken during the electrode implantation surgery.

2.6. Intracranial EEG (iEEG) recordings

The intracranial EEG (iEEG) data was recorded with a digital sampling frequency of 2,000 Hz using the Nihon Kohden Systems (Neurofax 1100A, Irvine, California, USA). For each participant, a consistent 90-minute EEG segment was chosen, ensuring it was at least two hours before or after any seizures, prior to tapering of anti-seizure medications, and before cortical stimulation mapping. This mapping usually took place two days post-implant. All the iEEG data used in the study were extracted from the clinical EEG recording.

2.7. Automated detection of High frequency oscillations

For the HFO analysis, a customized average reference was applied, which involved excluding electrodes that exhibited significant artifacts (Nariai et al. 2019). Two sets of candidate interictal HFOs were identified using the STE detector (Staba et al. 2002) and the MNI detector (Zelmann et al. 2009). HFOs were defined as spontaneous EEG patterns in the frequency range of 80-500 Hz, consisting of at least four oscillations that can be distinguished from the background. The STE detector (Staba et al. 2002) uses a sliding window approach to detect segments in the EEG signal as candidate interictal HFOs. The root mean square (RMS) energy of the segment under consideration is compared with a

global energy threshold that is computed from the sequence of the RMS values of the entire EEG signal. In contrast, the MNI detector (Zelmann et al. 2009) takes a more localized approach and detects HFO segments by comparing them with the surrounding baseline activity. The MNI detector consists of a baseline detector block and an energy-based event detector block. The baseline detector block identifies the baseline segments in the EEG, and the event detector block identifies the HFO segments using the energy threshold computed using the baseline segments. The detected baselines characterizes the background activity and plays an important role in channels where a large number of interictal epileptiform discharges (IED) are present. From this point onwards, we will refer to the set of candidate interictal HFOs detected by the STE and the MNI detector as STE set and MNI set, respectively. This study used the Matlab code and their default detector settings on RippleLab software (Navarrete et al. 2016).

2.8. Creation of each HFO set and subsequent training of deep learning-based classification (Figure 1: study workflow)

2.8.1. The Jaccard similarity between two detected HFO events (Figure 1. A)

—Assume there are two detected HFO events, represented by a tuple of start and end times, (s_1,e_1) and (s_2,e_2). Without loss of generality, we can assume that $s_1 < s_2$. Then, we define the Jaccard similarity between the two detected HFO events $d(s_1,s_2,e_1,e_2)$ in the following manner (see the study workflow):

- If $e_2 < e_1$, the detected HFO_2 is a subset of the detected HFO_1, then we set the Jaccard similarity $d(s_1,s_2,e_1,e_2) = 1$
- If $s_2 > e_1$, the two detected HFOs are disjoint, then we set the Jaccard similarity $d(s_1,s_2,e_1,e_2) = 0$
- If $e_2 > e_1$, and $e_1 > s_2$, the two detected HFOs have partial overlap, and then we set the Jaccard similarity $d(s_1,s_2,e_1,e_2) = (e_1\text{-}s_2)/(e_2\text{-}s_2)$

2.8.2. Decomposition of STE and MNI set into three disjoint sets (Figure 1. B)

—We used the Jaccard similarity metric to decompose the STE and MNI set into three disjoint sets of HFOs: the set of HFOs that are detected by both the STE and MNI detector (Intersection set), the set of HFOs that are detected by the MNI detector but missed by the STE detector (MNI only set) and the set of HFOs that are detected by STE detector but missed by the MNI detector (STE only set).

We populated the three disjoint sets using an algorithm described below:

- Step 1: For each HFO in the MNI set (s_{MNI},e_{MNI}), we compute its Jaccard similarity to all the HFOs detected by the STE detector and sort them in descending order
- Step 2: If there is an HFO in the STE set, (s_{STE},e_{STE}), with a Jaccard similarity greater than 0.95, then we place both the HFOs (s_{MNI},e_{MNI}) and (s_{STE},e_{STE}) in the Intersection set. If there is no HFO in the STE set with a Jaccard similarity greater than 0.95, then we place the HFO (s_{MNI},e_{MNI}) in the MNI only set.

- Step 3: Keep repeating Steps 1 and 2 until all the HFOs in the MNI set have been placed in either the Intersection or the MNI only set.
- Step 4: The HFOs in the STE set that have not been placed in the intersection set are used to populate the STE only set

The empirical distribution of Jaccard similarity scores was bimodal with two peaks at 0 and 1, prompting us to use a strict threshold of 0.95 for our greedy algorithm.

2.8.3. Training epileptogenic HFO (eHFO) detector (Figure 1. C/D)—We introduced the class of eHFOs, which aimed to capture HFOs generated from the epileptogenic tissues of the brain (Zhang et al. 2022b). It is obtained by training a DL-based detector for the HFOs that are distinctively present in the SOZ channels and other resection channels in post-operative seizure free patients. Since it is a data-driven procedure, the exact DL model is a function of the type of HFO detector. A defining characteristic of such data-driven eHFOs — irrespectively of the type of the HFOs used — is high amplitude in time-frequency plots across frequency bands at HFO onset (the inverted T-shaped template) (Hoogteijling et al. 2022).

The HFOs obtained by running the 90-minute intracranial EEG data through the STE and MNI detector were passed through the decomposition block to obtain the three disjoint HFO sets: MNI only set, Intersection set, and the STE only set. We constructed the Union HFO set by taking the Union of the three disjoint sets (MNI only + Intersection + STE only). Similarly, we constructed the MNI HFO set by taking the Union of Intersection and MNI only sets (Intersection + MNI only). A pre-trained artifacts detector (Zhang et al. 2022b) was used to filter the artifacts in the HFO set. We adopted the same structure of DL input and training strategy (weak supervision) as performed in the prior studies (Zhang et al. 2022a; Zhang et al. 2022b). In short, we extracted three features from each HFO in the set as our prior studies (Zhang et al. 2022a; Zhang et al. 2022b): i) a time-frequency plot (scalogram) generated using continuous Gabor wavelet transforms ranging from 10-500 Hz, ii) an EEG-tracing plot generated on a 2000 x 2000 image by scaling the time-series signal into the 0-2000 range to represent the EEG waveform's morphology, iii) an amplitude-coding plot generated to represent the relative amplitude of the time series signal: for every time point, the pixel intensity of a column of the image represented the signal's raw value at that time. These three images were resized into the standard size (224 x 224), serving as the input to the neural network. We adopted a weak labeling scheme to generate the labels for each HFO: HFOs in the set that originated from the resected channels (obtained from the channel status) were assigned a label of 1, and HFOs in the set that originated from the preserved channels (obtained from the channel status) were assigned a label of 0. The extracted features and the weak labels were then used to train a state-of-the-art DL model, namely ResNet-18 (He et al. 2016). Each of the three different detectors was trained by each training set: Union eHFO detector trained with Union HFO set, MNI eHFO detector trained with MNI set, and STE eHFO detector trained with STE set.

A patient-wise elimination training strategy was adopted to validate the findings of the detectors and generate the receiver operating characteristics curve. In this training strategy, we trained ten models in total: one model each for the seizure-free patients (9 seizure-free

patients) and one model for the non-seizure-free patients. The model for a seizure-free patient was trained by excluding the iEEG data of that seizure-free patient from the training set. For example, we trained a model for a particular patient by constructing the training set from iEEG data of the remaining 8 seizure-free patients. The model for the non-seizure-free patients was trained by constructing the training set from iEEG data of the 9 seizure-free patients. In the inference stage, we used the patient-wise models to predict the outcome of the seizure-free patients and the non-seizure-free model to predict the outcome of the non-seizure-free patients. Therefore, we are using an independent cohort of EEGs to validate the findings of the detectors, as there is no overlap between the training and test set.

2.9. Evaluating the performance of eHFO detectors in predicting postoperative seizure outcomes

The trained eHFO detectors were used to classify the HFOs in the Union HFO set into epileptogenic HFOs (eHFO) and non-epileptogenic HFOs (non-eHFO). The ratio of the rates of eHFO in the resected region to the preserved region was used as a feature to train a logistic regression model for predicting the postoperative seizure outcomes of 15 patients. By varying the classification threshold on the ratio, a receiver operating characteristics curve (ROC) was generated. The area under the ROC curve was computed and used as a metric to evaluate the performance of the eHFO detectors in predicting the postoperative seizure outcome (seizure freedom at 24 months after surgery) of patients.

2.10. Time-frequency plot characteristics of the HFOs in the three HFO sets

We computed the mean time-frequency scalogram of HFOs in the three sets (Intersection, MNI only, STE only) by averaging the power across all the scalograms of HFOs in the sets. The mean scalograms were then compared across the three sets in four distinct frequency bands (10-30 Hz, 30-80 Hz, 80-250 Hz, 250-500 Hz) by performing a t-test between the mean scalograms. We also created a customized scalogram, using the same technique as in our previous work (Zhang et al. 2022b), to visually represent the frequency ranges in which the scalograms of the HFOs belonging to different sets varied in. For every pixel (x,y) in the 224*224 image, we created two sets of data points: Sint(x,y) and Smni(x,y), where Sint(x,y) consists of the intensity values of the scalogram of the HFOs in the Intersection set and Smni(x,y) consists of the intensity values of the scalogram of the HFOs in the MNI only set. Then we performed one-tailed t-tests to determine whether a random variable A(x,y), whose samples are given by Sint(x,y), is greater than that of a random variable B(x,y) whose samples are given by Smni(x,y). If this hypothesis is found to be true, with a p-value less than 0.001, we set the pixel value I(x,y) = 1; otherwise, I(x,y) = 0. Similarly, by following the above procedure, we compared the time-frequency scalogram of HFOs in the MNI only, and the STE only sets with two sets of data points: Smni(x,y) and Sste(x,y).

2.11. Distribution of HFO with spike and epileptogenic HFO in three HFO sets

We passed the three HFO sets (Intersection, MNI only, STE only) through the trained spike detector (Zhang et al. 2022b) to classify them into HFOs with spikes (spk-HFO) and HFOs without spikes (non-spk-HFO) categories. Similarly, we passed the three HFO sets through the trained union eHFO detector to classify them into eHFO and non-eHFO categories. We compared the distribution of HFO with spike and eHFO across the three HFO sets.

2.12. Relationship between epileptogenic HFOs and HFOs with spikes

We passed the Union HFO set through the three trained eHFO detectors (Union, MNI, and STE) to classify the HFOs into eHFO and non-eHFO categories. We also passed the Union HFO set through the trained spike detector to classify the HFOs into HFOs with spikes (spk-HFO) and HFOs without spikes (non-spk-HFO) categories. For each eHFO detector type, we computed the overlap between the eHFO and spk-HFO set and then compared the overlap across the three eHFO detectors.

2.13. Statistical analysis

We used Python (version 3.7.3; Python Software Foundation, USA) for above mentioned statistical calculations. PyTorch (version 1.6.0; Facebook's AI Research lab) was used to develop the deep neural network. Quantitative measures are described by medians with interquartile or mean with standard deviations. Comparisons between groups were performed using chi-square for comparing two distributions and Student's t-test for quantitative measures (in means with standard deviations). All comparisons were two-sided, and significant results were considered at $p < 0.05$ unless stated otherwise. The particular statistical tests executed for each experiment are detailed in their respective sections.

2.14. Data sharing and availability of the methods

The anonymized EEG data utilized in this research can be obtained by sending a reasonable request to the corresponding author. The Python-based code employed for this study can be freely accessed at (https://github.com/roychowdhuryresearch/HFO-Classification). Individuals can use this to train and test the deep learning algorithm on their own data, thus validating the effectiveness and usefulness of our methods.

3. RESULTS:

3.1. Patients' characteristics:

There were 15 patients (8 females) enrolled during the study period. The median age at surgery was 13 years (range: 3-20 years). The median electrocorticography monitoring duration was four days (range: 2-12 days), and the median number of seizures captured during the monitoring was 7 (range: 1-35). All 15 patients underwent resection immediately following intracranial monitoring and provided postoperative seizure outcomes at 24 months (9 of 15 became seizure-free). Details of patients' clinical information are listed in Table 1.

3.2. Interictal HFO detection and HFOs' classification

A total of 105622 HFOs were detected with the STE detector and 47143 with the MNI detector in 90-minute EEG data from the 15 patients. Of those, 29668 were the Intersection set. After artifact rejection, there were 84602 HFOs detected with the STE detector, 34965 with the MNI detector and 21248 of them belonged to the Intersection set. We classified the HFOs in the three sets (Intersection, MNI only, and STE only) into HFOs with spikes and HFOs without spikes. Across 15 patients, on average, 88% of HFOs in the Intersection set were HFOs with spikes, 87% of HFOs in the MNI only set were HFOs with spikes, and 36% of HFOs in the STE only set were HFOs with spikes. The percentage of HFO with spikes

was significantly higher in the Intersection and the MNI only set when compared to the STE only set (Intersection vs. STE only: mean 0.88 versus 0.36, $p < 0.001$; MNI only vs. STE only: mean 0.87 versus 0.36, $p < 0.01$) (Figure 2).

3.3. Spectral Characteristics of HFOs in three HFO sets

The analysis of the mean time-frequency map averaged across the 15 patients demonstrated that HFOs in the Intersection set showed higher amplitude in all the frequency bands (fast ripple: 250-500 Hz; ripple: 80-250 Hz; gamma: 30-80; and beta: 10-30 Hz) than HFOs in the MNI only or STE only set ($p < 0.0001$ for all comparisons). However, comparisons of the amplitude between the MNI only and the STE only HFOs did not show differences in fast ripple, ripple, and gamma bands ($p = 0.90$, 0.99, and 0.99, respectively). In the beta band, HFOs in the MNI only set have more amplitude than the ones in the STE only set ($p < 0.001$) (Figure 3A). With more detailed pixel-by-pixel analysis, we demonstrated that the HFOs in the Intersection set had higher amplitude than HFOs in the MNI only set in all four frequency bands, with a noticeable difference in the 30-80 Hz and 80-250 Hz frequency bands. Similarly, HFOs in the MNI only set have higher amplitude than HFOs in the STE only set in the 10-30 Hz and 30-80 Hz frequency bands, with a significant difference in the 10-30 Hz frequency band (Figure 3B).

3.4. Overlap between eHFOs and HFOs with spikes in three eHFO detectors

We classified the HFOs in the Union HFO set (Intersection + MNI only + STE only) into HFOs with spikes and HFOs without spikes. We also classified the HFOs in the Union HFO set into eHFOs and non-eHFOs using the three types of eHFO detectors (Union, MNI, and STE). Across the 15 patients, there was an overlap ratio of 0.79, 0.95, and 0.78 between HFOs with spikes and eHFOs with the Union, MNI, and STE eHFO detectors, respectively. The overlap percentage was significantly higher in the MNI HFOs than in the Union and STE HFOs (MNI vs. Union: mean 0.95 vs. 0.79, $p < 0.001$; MNI vs. STE: mean 0.95 vs. 0.78, $p < 0.001$). There were no significant differences in the overlap percentage when comparing the Union and STE HFOs (Union vs. STE: mean 0.79 vs. 0.78, $p = 0.042$, which became insignificant after Bonferroni correction) (Figure 4).

3.5. Characteristic differences of eHFOs vs. non-eHFOs controlled by spike status

We investigated the differences in the time-frequency characteristics between eHFOs and non-eHFOs controlled by spike status. Across four frequency bands, eHFOs with spikes showed higher power than non-eHFOs with spikes, and eHFOs without spikes showed higher power than non-eHFOs without spikes ($p < 0.0001$ in all comparisons with Welch t-test with unequal variances). (Figure 5)

3.6. Distribution of eHFO in three HFO sets

We classified the HFOs in the three sets (Intersection, MNI only, and STE only) into eHFOs and non-eHFOs using the Union eHFO detector. Across 15 patients, on average, 82%, 85%, and 45% of HFOs in the Intersection set, MNI only set, and STE only set were eHFOs, respectively. The percentages of eHFOs were significantly higher in the Intersection, and MNI only set when compared to the STE only set (Intersection vs. STE only: mean 82%

versus 45%, $p < 0.001$; MNI only vs. STE only: mean 85% versus 45%, $p = 0.03$). We plotted the distribution of the confidence scores (the probability of each HFO being eHFO) returned by the Union eHFO detector for the three sets. The distribution for the Intersection and the MNI only set was skewed towards 1 (higher confidence towards eHFO), while the STE only set showed a more balanced distribution (Figure 6).

3.7. Predicting postoperative seizure outcomes using HFO resection ratios

We used the HFO and eHFO resection ratio (ratio = total number of resected HFOs/ total number of detected HFOs) as a classifier to predict the postoperative seizure outcomes. Three types of HFO detectors (Union, MNI, and STE) were used for computing the ratios. For both cases (HFO and eHFO resection ratios), the Union HFO detector achieved the best performance in predicting the postoperative seizure outcome (AUC of 0.78 and 0.89), followed by the MNI HFO detector (AUC of 0.76 and 0.85), and then the STE eHFO detector (AUC of 0.72 and 0.81) (Figure 7).

3.8. Post-hoc sensitivity analysis

We conducted a post-hoc sensitivity analysis to prove that the superior performance of the Union eHFO detector was not due to biased HFO samples. We trained the STE and the Union eHFO detector using the same number of training samples (n = 84602). In training the STE eHFO detector, the training set only consisted of HFO samples from the STE set. In training the Union eHFO detector, the training set consisted of an equal number of HFO samples from the STE and MNI set. The trained models were then used to predict the patient outcomes and generate receiver operating characteristics (ROC) curves. We plotted the area under the ROC curve (AUC) as a function of the number of training samples used to train the detectors. From the plot, it can be observed that there is a significant gap between the curves showing that even for the same number of training samples union eHFO detector performs better in terms of predicting the seizure outcomes (Supplementary Data).

4. DISCUSSION:

Although HFOs are widely investigated as one of the spatial biomarkers of the EZ, the definition of what constitutes an HFO event is computational and algorithm-dependent (Frauscher et al. 2017; Remakanthakurup Sindhu et al. 2020). There have been some efforts at comparing the signal characteristics of the two widely used detectors, namely the MNI and the STE detectors; for example, the study (Zelmann et al. 2010) that introduced the MNI detector, showed it could detect HFO events in EEG data with noisy background (based on the baseline adjustment principle) that were often missed by the STE detector (Zelmann et al. 2012). However, this does not answer whether the MNI detector—which has more stringent settings—also misses the detection of certain physiological and pathological HFOs that could have clinical impact. Thus, a comprehensive study comparing the signal and morphological differences of STE and MNI HFOs, especially in the context of pathological HFOs, is needed. In this study, we first verified that, even at the level of individual subjects, each detector produced unique HFO events not detected by the other (referred to as MNI only and STE only HFO sets, respectively) while sharing an intersection set of HFOs (Intersection-set HFOs). We further showed that the Intersection set HFOs, which were

detected by both detectors, contained most pathological features demonstrated by high association rates with spikes and their signal characteristics being consistent with eHFOs (high amplitude in time-frequency plots across frequency bands at HFO onset) as reported in our previous study (Zhang et al. 2022b). The MNI HFOs were more biased towards HFOs with spikes and eHFOs and the STE HFOs were more biased towards HFOs without spikes and non-eHFOs. However, both the MNI only and STE only HFO sets contained significant number of pathological HFOs (for example, the STE only HFO set has 36% of total spk-HFO that are thus missed by the MNI detector). Thus the Union eHFO detector that processes all the HFOs by either the MNI or the STE detector could potentially better capture the characteristics of HFOs that are distinctively present in EZ. We then created three different eHFO detectors namely Union eHFO, STE eHFO, and MNI eHFO. Indeed, we demonstrated that (i) using any eHFO resection ratio outperformed the unclassified HFO resection ratio in any HFO detection method in post operative seizure outcome prediction; (ii) the Union eHFO detector outperformed all other detectors in postoperative seizure outcome prediction.

Our findings are clinically meaningful. We presented the data to show that neither the MNI nor the STE detector is sensitive enough to evaluate pathological HFOs. When we use HFO evaluation in clinical context, we might consider using several types of detection methods, as proposed in our study, to enhance the sensitivity of the detection. In addition, not all detected HFOs are pathological. In a recent clinical trial and observational study, issues with the feasibility of utilizing HFOs in clinical settings were elucidated (Jacobs et al. 2018; Zweiphenning et al. 2022). These included the time constraints of expert-based visual analysis in detecting and classifying HFOs (artifacts, pathological HFOs, and physiological HFOs). Automated and reproducible detection and classification of HFOs will be crucial to use HFOs in clinical practice. In our more recent work, data from cortical stimulation mapping were used to characterize HFOs with origin in the eloquent cortex and hence, physiological in origin (Zhang et al. 2022a). If HFOs can be automatically classified into such HFOs that are expressed in the eloquent cortex, then one can start localizing the eloquent cortex from HFO detections, which would have a significant clinical impact. Since the STE detector can detect many more of such physiological HFOs than the MNI detector, it further underscores the need for using both detectors and then designing DL-assisted classifiers to automatically extract clinically relevant information.

Given that discovering the characteristics of pathological HFOs is an active area of research, we now discuss the relationship of such work with our findings. For example, HFOs with higher amplitude are hypothesized to be characteristics of pathological HFOs (Charupanit et al. 2020). Similarly, HFOs with spikes are believed to be correlated with the pathological nature of HFOs (Weiss et al. 2016). Our study also substantiated such findings as we observed that the Intersection-set HFOs had higher amplitude in all the frequency bands and a high spike association rate. We further investigated characterizations of pathological HFOs using a DL based data-driven approach as introduced in our recent work (Zhang et al. 2022a), where no *a priori* feature engineering is required to train the algorithms. In particular, data from patients who became seizure-free post-surgery was used to characterize HFOs into eHFOs and non-eHFOs. Such eHFOs were shown to share known characteristics of pathological HFOs (Zhang et al. 2022b). Thus, data obtained from post operative seizure

free patients along with DL can be used to automatically distill manually defined HFOs to provide clinically useful localization information about EZ, and thus obtain automatic characterizations of pathological HFOs. Future studies utilizing larger datasets and more sophisticated DL-architectures may further characterize pathological and physiological HFOs (Hoogteijling et al. 2022).

There are several limitations to our study. We only tested the STE and MNI detection methods of HFO analysis. We plan to investigate other methodologies, such as short line length (SLL) (Gardner et al. 2007) and Hilbert detections (Crepon et al. 2010). The iEEG data was recorded by placing intracranial strips and grid electrodes. Although we expect the analysis to hold in a clinical setting where the data is recorded using stereotactic EEG (sEEG), the analysis and the deep learning model need to be validated on a dataset of sEEG recordings. Another potential limitation of our study is the diversity of the dataset in terms of the number of patients, age group of the patients, state of the patients (we analyzed sleep segment only), and the duration of the EEG recordings. We used EEG data from non-REM sleep, as pathological HFOs were more commonly detected during this state (von Ellenrieder et al. 2017). Awake EEG data can be affected by many factors, such as subjects' motion, thus we did not prepare such a dataset. Since the morphology of the detections might be affected by the age and vigilance state of the patients, the transferability of the analysis and the model needs to be verified in a larger cohort of patients with a diversified age range, vigilance state, and epilepsy etiology.

Supplementary Material

Refer to Web version on PubMed Central for supplementary material.

ACKNOWLEDGMENT:

The authors have no conflict of interest to disclose. HN is supported by the National Institute of Neurological Disorders and Stroke (NINDS) K23NS128318, the Sudha Neelakantan & Venky Harinarayan Charitable Fund, the Elsie and Isaac Fogelman Endowment, and the UCLA Children's Discovery and Innovation Institute (CDI) Junior Faculty Career Development Grant (#CDI-TTCF-07012021). AD is supported to research abroad by the Uehara Memorial Foundation and SENSHIN Medical Research Foundation. SAH has received research support from the Epilepsy Therapy Project, the Milken Family Foundation, the Hughes Family Foundation, the Elsie and Isaac Fogelman Endowment, Eisai, Lundbeck, Insys, Zogenix, GW Pharmaceuticals, UCB, and has received honoraria for service on the scientific advisory boards of Questcor, Mallinckrodt, Insys, UCB, and Upsher-Smith, for service as a consultant to Eisai, UCB, GW Pharmaceuticals, Insys, and Mallinckrodt, and for service on the speakers' bureaus of Mallinckrodt and Greenwich Bioscience. RS serves on scientific advisory boards and speakers bureaus and has received honoraria and funding for travel from Eisai, Greenwich Biosciences, UCB Pharma, Sunovion, Supernus, Lundbeck Pharma, Liva Nova, and West Therapeutics (advisory only); receives royalties from the publication of Pellock's Pediatric Neurology (Demos Publishing, 2016) and Epilepsy: Mechanisms, Models, and Translational Perspectives (CRC Press, 2011). RJS is supported by the National Institute of Neurological Disorders and Stroke (NINDS) R01NS106957. We are indebted to Joyce H. Matsumoto, Lekha M. Rao, Rajsekar R. Rajaraman, Maria Garcia Roca, Richard Le, Patrick Wilson, Cesar Dominguez and Jimmy C Nguyen for their assistance in the study and sample acquisition.

REFERENCES:

Akiyama T, McCoy B, Go CY, Ochi A, Elliott IM, Akiyama M, Donner EJ, Weiss SK, Snead OC 3rd, Rutka JT, Drake JM, and Otsubo H. 2011. 'Focal resection of fast ripples on extraoperative intracranial EEG improves seizure outcome in pediatric epilepsy', Epilepsia, 52: 1802–11. [PubMed: 21801168]

Bragin A, Engel J Jr., Wilson CL, Fried I, and Mathern GW. 1999a. 'Hippocampal and entorhinal cortex high-frequency oscillations (100--500 Hz) in human epileptic brain and in kainic acid--treated rats with chronic seizures', Epilepsia, 40: 127–37. [PubMed: 9952257]

Bragin A, Engel J Jr., Wilson CL, Vizentin E, and Mathern GW. 1999b. 'Electrophysiologic analysis of a chronic seizure model after unilateral hippocampal KA injection', Epilepsia, 40: 1210–21. [PubMed: 10487183]

Charupanit K, Sen-Gupta I, Lin JJ, and Lopour BA. 2020. 'Amplitude of high frequency oscillations as a biomarker of the seizure onset zone', Clin Neurophysiol, 131: 2542–50. [PubMed: 32927209]

Crepon B, Navarro V, Hasboun D, Clemenceau S, Martinerie J, Baulac M, Adam C, and Le Van Quyen M. 2010. 'Mapping interictal oscillations greater than 200 Hz recorded with intracranial macroelectrodes in human epilepsy', Brain, 133: 33–45. [PubMed: 19920064]

Frauscher B, Bartolomei F, Kobayashi K, Cimbalnik J, van 't Klooster MA, Rampp S, Otsubo H, Holler Y, Wu JY, Asano E, Engel J Jr., Kahane P, Jacobs J, and Gotman J. 2017. 'High-frequency oscillations: The state of clinical research', Epilepsia, 58: 1316–29. [PubMed: 28666056]

Frauscher B, von Ellenrieder N, Zelmann R, Rogers C, Nguyen DK, Kahane P, Dubeau F, and Gotman J. 2018. 'High-Frequency Oscillations in the Normal Human Brain', Ann Neurol, 84: 374–85. [PubMed: 30051505]

Gardner AB, Worrell GA, Marsh E, Dlugos D, and Litt B. 2007. 'Human and automated detection of high-frequency oscillations in clinical intracranial EEG recordings', Clin Neurophysiol, 118: 1134–43. [PubMed: 17382583]

Guth TA, Kunz L, Brandt A, Dümpelmann M, Klotz KA, Reinacher PC, Schulze-Bonhage A, Jacobs J, and Schönberger J. 2021. 'Interictal spikes with and without high-frequency oscillation have different single-neuron correlates', Brain, 144: 3078–88. [PubMed: 34343264]

He K, Zhang X, Ren S, and Sun J. 2016. 'Deep residual learning for image recognition.', Proceedings of the IEEE conference on computer vision and pattern recognition: 770–78.

Hoogteijling S, and Zijlmans M. 2022. 'Deep learning for epileptogenic zone delineation from the invasive EEG: challenges and lookouts', Brain Commun, 4: fcab307. [PubMed: 35169704]

Jacobs J, Wu JY, Perucca P, Zelmann R, Mader M, Dubeau F, Mathern GW, Schulze-Bonhage A, and Gotman J. 2018. 'Removing high-frequency oscillations: A prospective multicenter study on seizure outcome', Neurology, 91: e1040–e52. [PubMed: 30120133]

Jacobs J, Zijlmans M, Zelmann R, Chatillon CE, Hall J, Olivier A, Dubeau F, and Gotman J. 2010. 'High-frequency electroencephalographic oscillations correlate with outcome of epilepsy surgery', Ann Neurol, 67: 209–20. [PubMed: 20225281]

Kuroda N, Sonoda M, Miyakoshi M, Nariai H, Jeong JW, Motoi H, Luat AF, Sood S, and Asano E. 2021. 'Objective interictal electrophysiology biomarkers optimize prediction of epilepsy surgery outcome', Brain Commun, 3: fcab042. [PubMed: 33959709]

Motoi H, Jeong JW, Juhasz C, Miyakoshi M, Nakai Y, Sugiura A, Luat AF, Sood S, and Asano E. 2019. 'Quantitative analysis of intracranial electrocorticography signals using the concept of statistical parametric mapping', Scientific Reports, 9: 17385. [PubMed: 31758022]

Nariai H, Hussain SA, Bernardo D, Fallah A, Murata KK, Nguyen JC, Rajaraman RR, Rao LM, Matsumoto JH, Lerner JT, Salamon N, Elashoff D, Sankar R, and Wu JY. 2019. 'Prospective observational study: Fast ripple localization delineates the epileptogenic zone', Clin Neurophysiol, 130: 2144–52. [PubMed: 31569042]

Nariai H, Nagasawa T, Juhasz C, Sood S, Chugani HT, and Asano E. 2011. 'Statistical mapping of ictal high-frequency oscillations in epileptic spasms', Epilepsia, 52: 63–74. [PubMed: 21087245]

Nariai H, Wu JY, Bernardo D, Fallah A, Sankar R, and Hussain SA. 2018. 'Interrater reliability in visual identification of interictal high-frequency oscillations on electrocorticography and scalp EEG', Epilepsia Open, 3: 127–32.

Navarrete M, Alvarado-Rojas C, Le Van Quyen M, and Valderrama M. 2016. 'RIPPLELAB: A Comprehensive Application for the Detection, Analysis and Classification of High Frequency Oscillations in Electroencephalographic Signals', PloS One, 11: e0158276. [PubMed: 27341033]

Nonoda Y, Miyakoshi M, Ojeda A, Makeig S, Juhasz C, Sood S, and Asano E. 2016. 'Interictal high-frequency oscillations generated by seizure onset and eloquent areas may be differentially coupled with different slow waves', Clin Neurophysiol, 127: 2489–99. [PubMed: 27178869]

Remakanthakurup Sindhu K, Staba R, and Lopour BA. 2020. 'Trends in the use of automated algorithms for the detection of high-frequency oscillations associated with human epilepsy', Epilepsia, 61: 1553–69. [PubMed: 32729943]

Rosenow F, and Luders H. 2001. 'Presurgical evaluation of epilepsy', Brain, 124: 1683–700. [PubMed: 11522572]

Spring AM, Pittman DJ, Aghakhani Y, Jirsch J, Pillay N, Bello-Espinosa LE, Josephson C, and Federico P. 2017. 'Interrater reliability of visually evaluated high frequency oscillations', Clin Neurophysiol, 128: 433–41. [PubMed: 28160749]

Staba RJ, Wilson CL, Bragin A, Fried I, and Engel J Jr. 2002. 'Quantitative analysis of high-frequency oscillations (80-500 Hz) recorded in human epileptic hippocampus and entorhinal cortex', Journal of Neurophysiology, 88: 1743–52. [PubMed: 12364503]

van 't Klooster MA, van Klink NE, Leijten FS, Zelmann R, Gebbink TA, Gosselaar PH, Braun KP, Huiskamp GJ, and Zijlmans M. 2015. 'Residual fast ripples in the intraoperative corticogram predict epilepsy surgery outcome', Neurology, 85: 120–8. [PubMed: 26070338]

von Ellenrieder N, Dubeau F, Gotman J, and Frauscher B. 2017. 'Physiological and pathological high-frequency oscillations have distinct sleep-homeostatic properties', Neuroimage Clin, 14: 566–73. [PubMed: 28337411]

Weiss SA, Orosz I, Salamon N, Moy S, Wei L, Van't Klooster MA, Knight RT, Harper RM, Bragin A, Fried I, Engel J Jr., and Staba RJ. 2016. 'Ripples on spikes show increased phase-amplitude coupling in mesial temporal lobe epilepsy seizure-onset zones', Epilepsia, 57: 1916–30. [PubMed: 27723936]

Wong SM, Arski ON, Workewych AM, Donner E, Ochi A, Otsubo H, Snead OC 3rd, and Ibrahim GM. 2021. 'Detection of high-frequency oscillations in electroencephalography: A scoping review and an adaptable open-source framework', Seizure, 84: 23–33. [PubMed: 33271473]

Worrell GA, Gardner AB, Stead SM, Hu S, Goerss S, Cascino GJ, Meyer FB, Marsh R, and Litt B. 2008. 'High-frequency oscillations in human temporal lobe: simultaneous microwire and clinical macroelectrode recordings', Brain, 131: 928–37. [PubMed: 18263625]

Wu JY, Sankar R, Lerner JT, Matsumoto JH, Vinters HV, and Mathern GW. 2010. 'Removing interictal fast ripples on electrocorticography linked with seizure freedom in children', Neurology, 75: 1686–94. [PubMed: 20926787]

Zelmann R, Mari F, Jacobs J, Zijlmans M, Chander R, and Gotman J. 2010. 'Automatic detector of high frequency oscillations for human recordings with macroelectrodes', Annu Int Conf IEEE Eng Med Biol Soc, 2010: 2329–33.

Zelmann R, Mari F, Jacobs J, Zijlmans M, Dubeau F, and Gotman J. 2012. 'A comparison between detectors of high frequency oscillations', Clin Neurophysiol, 123: 106–16. [PubMed: 21763191]

Zelmann R, Zijlmans M, Jacobs J, Châtillon CE, and Gotman J. 2009. 'Improving the identification of High Frequency Oscillations', Clin Neurophysiol, 120: 1457–64. [PubMed: 19576848]

Zhang Y, Chung H, Ngo JP, Monsoor T, Hussain SA, Matsumoto JH, Walshaw PD, Fallah A, Sim MS, Asano E, Sankar R, Staba RJ, Engel J, Speier W, Roychowdhury V, and Nariai H. 2022a. 'Characterizing physiological high-frequency oscillations using deep learning', J Neural Eng, 19.

Zhang Y, Lu Q, Monsoor T, Hussain SA, Qiao JX, Salamon N, Fallah A, Sim MS, Asano E, Sankar R, Staba RJ, Engel J Jr., Speier W, Roychowdhury V, and Nariai H. 2022b. 'Refining epileptogenic high-frequency oscillations using deep learning: a reverse engineering approach', Brain Commun, 4: fcab267. [PubMed: 35169696]

Zijlmans M, Jacobs J, Zelmann R, Dubeau F, and Gotman J. 2009. 'High-frequency oscillations mirror disease activity in patients with epilepsy', Neurology, 72: 979–86. [PubMed: 19289737]

Zweiphenning W, Klooster MAV, van Klink NEC, Leijten FSS, Ferrier CH, Gebbink T, Huiskamp G, van Zandvoort MJE, van Schooneveld MMJ, Bourez M, Goemans S, Straumann S, van Rijen PC, Gosselaar PH, van Eijsden P, Otte WM, van Diessen E, Braun KPJ, and Zijlmans M. 2022. 'Intraoperative electrocorticography using high-frequency oscillations or spikes to tailor epilepsy surgery in the Netherlands (the HFO trial): a randomised, single-blind, adaptive non-inferiority trial', Lancet Neurol, 21: 982–93. [PubMed: 36270309]

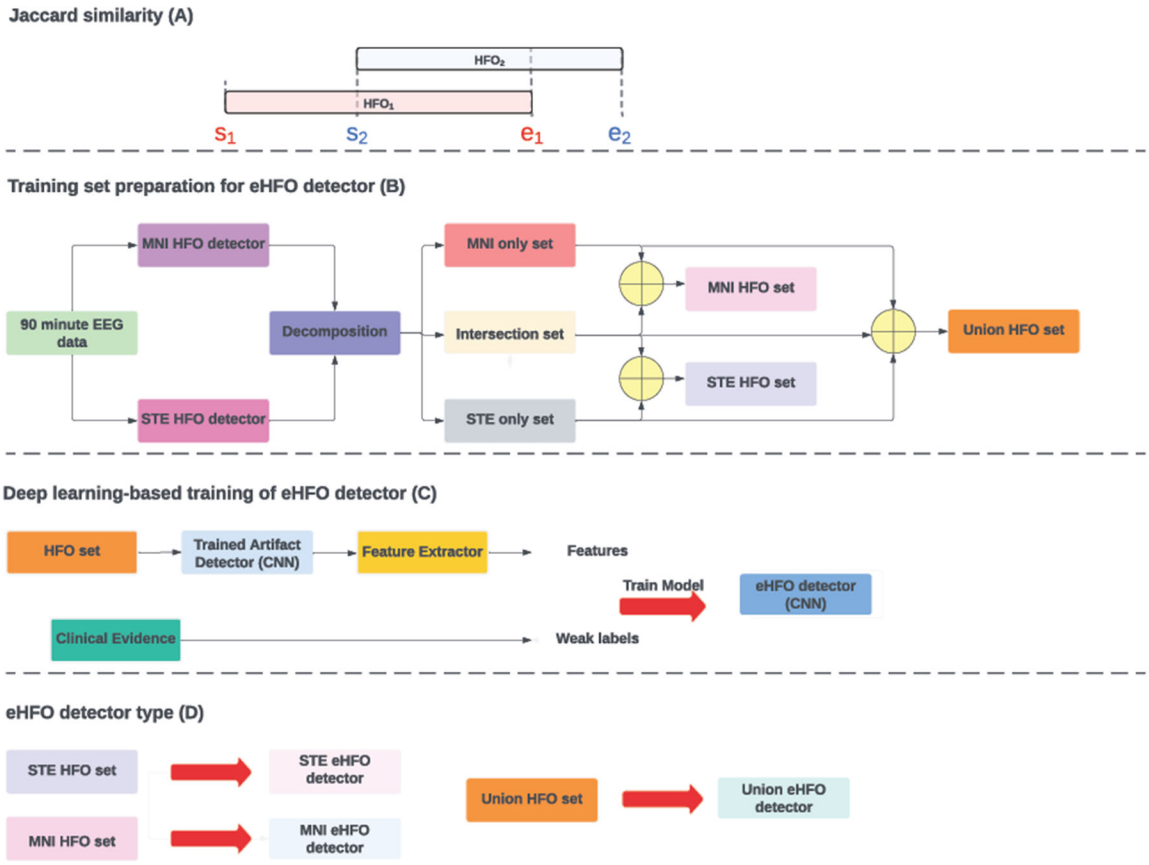

Figure 1: Study workflow

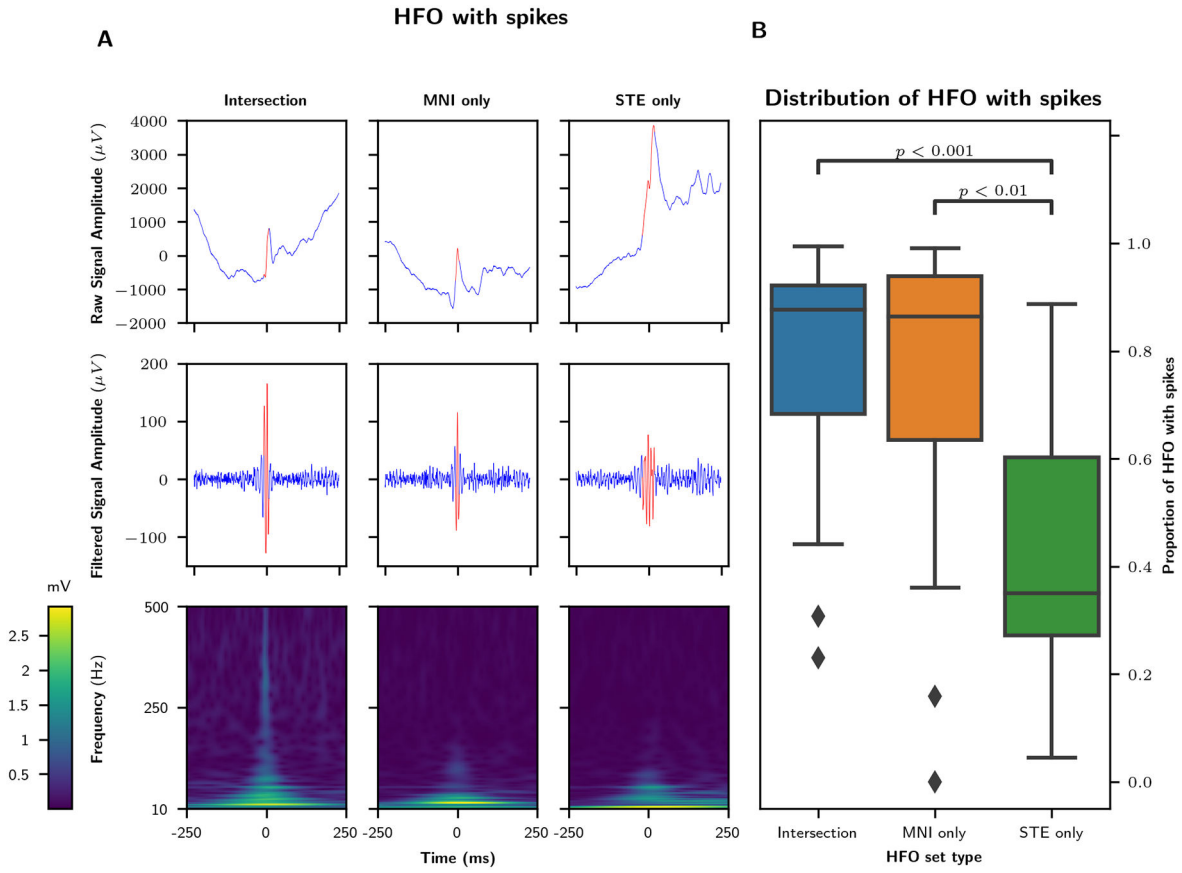

Figure 2: Distribution of HFOs with spikes in three HFO sets:

(A) An example of HFO with spike from each HFO set (Intersection, MNI only, and STE only) is shown. The first row shows the original tracing, the second row shows the filtered tracing (80-500 Hz), and the third shows the time-frequency plot. (B) The proportion of HFO with spikes in 15 patients is plotted as box plots and labeled by the HFO set type. Across a patient body of 15 patients, the Intersection set has the highest proportion of HFO with spikes on average, followed by the MNI and STE only set. The proportion of HFOs with spikes was significantly higher in the Intersection, and MNI only set compared to the STE only set (Intersection vs. STE only: mean 0.88 versus 0.36, $p < 0.001$; MNI only vs. STE only: mean 0.87 versus 0.36, $p < 0.01$).

HFOs: high-frequency oscillations; MNI: Montreal Neurological Institute (detector); STE: Short-term energy.

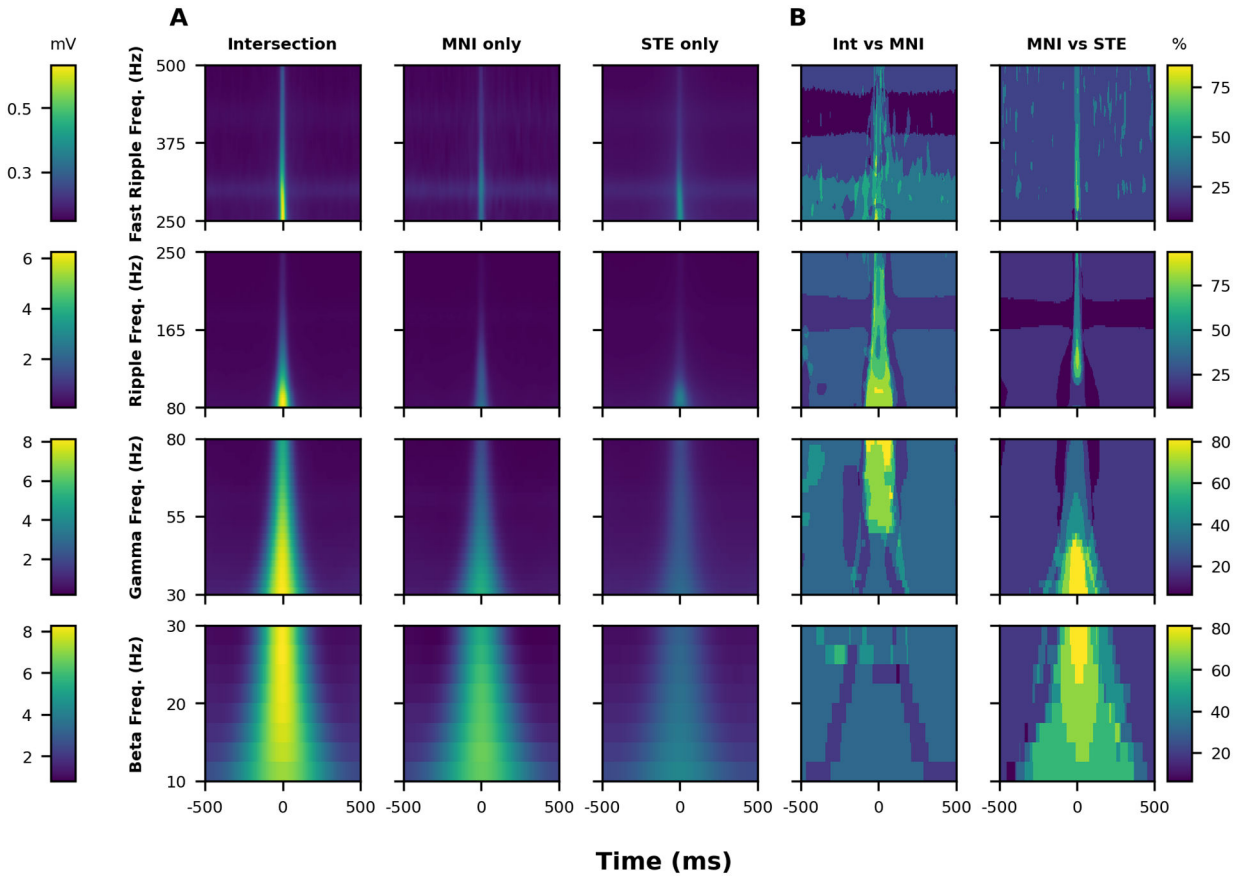

Figure 3. Time-frequency plot characteristics of HFOs in three HFO sets:

(A) The time-frequency plots of HFOs, averaged across all patients (n=15), are plotted and labeled based on their set type and four distinct frequency bands. Across four frequency bands, HFOs in the Intersection set have higher amplitude than HFOs in the MNI only set and STE only set. HFOs in the MNI only set have higher amplitude than STE only set in the 10-30 and 30-80 Hz frequency bands. (B) Pixel-wise analysis of time-frequency plot amplitude differences among three HFO sets: We created a custom scalogram to visually represent the frequency ranges where the HFOs belonging to different sets varied. The lighter-colored regions in the figure indicate pixels where the mean amplitude of one HFO set is statistically higher (p-value below 0.005 from a one-tailed t-test) than the other HFO set. From the left plot, it is clear that the HFOs in the Intersection set have higher amplitude than HFOs in the MNI only set in all four frequency bands, with a noticeable difference in the 30-80 Hz and 80-250 Hz frequency bands. Similarly, the right plot shows that HFOs in the MNI only set have higher amplitude than HFOs in the STE only set in the 10-30 Hz and 30-80 Hz frequency bands, with a significant difference in the 10-30 Hz frequency band. HFOs: high-frequency oscillations; MNI: Montreal Neurological Institute (detector); STE: Short-term energy.

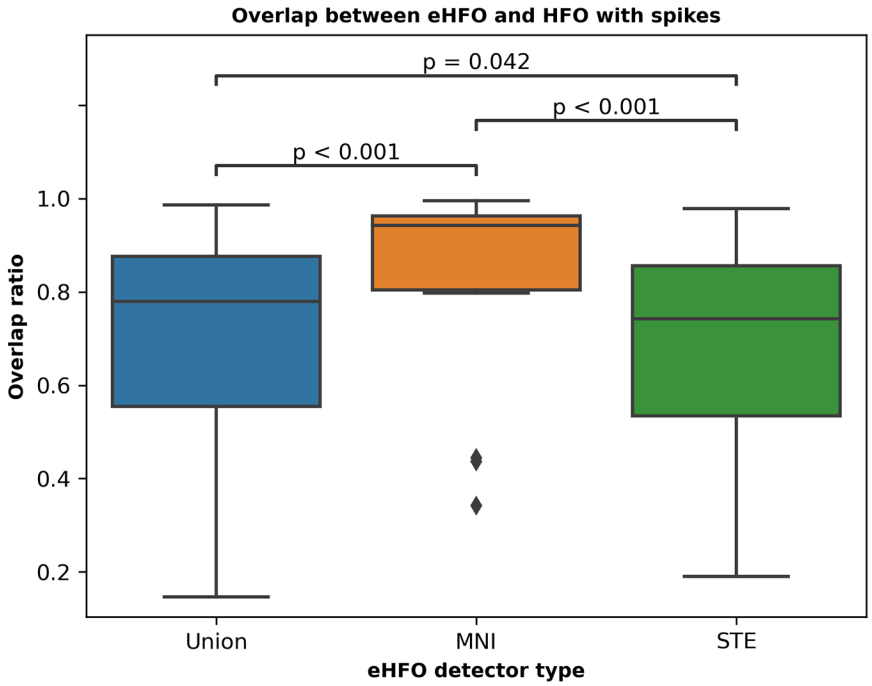

Figure 4. Overlap between eHFO and HFO with spike set in three eHFO detectors:

The overlap ratio between eHFO and HFO with spike set in 15 patients is plotted as box plots and labeled by the eHFO detector type. Across the cohort of 15 patients, there was significant overlap between the eHFOs and HFOs with spikes for all three eHFO detectors. The overlap ratio was significantly higher in the MNI eHFO detector when compared to the Union and STE eHFO detectors (MNI vs. Union: mean 0.95 versus 0.79, $p < 0.001$; MNI vs. STE: mean 0.95 versus 0.78, $p < 0.001$) while there was no significant difference in the overlap ratio between Union and STE eHFO detectors (Union vs. STE: mean 0.79 versus 0.78, $p = 0.042$).

HFOs: high-frequency oscillations; eHFOs: epileptogenic HFOs; MNI: Montreal Neurological Institute (detector); STE: Short-term energy.

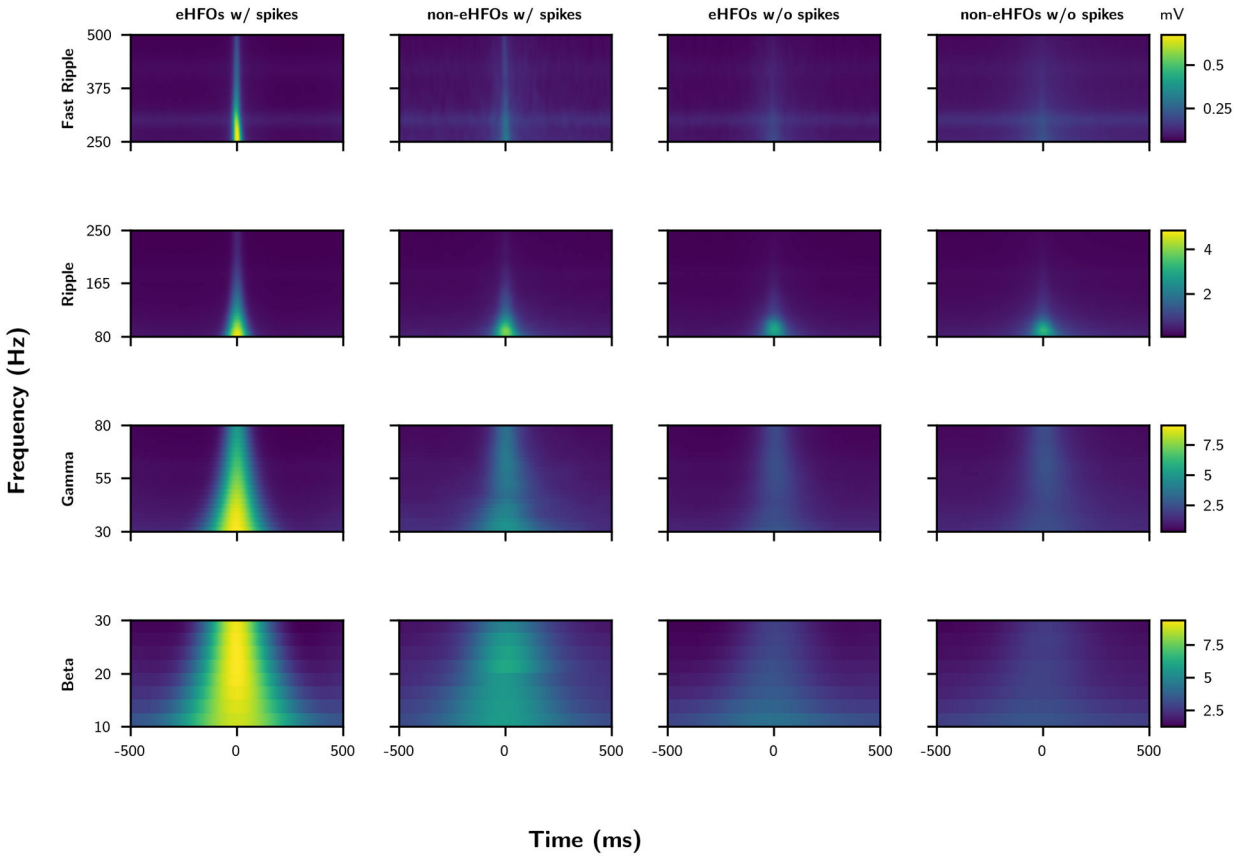

Figure 5. Time-frequency plot characteristics of eHFOs vs. non-eHFOs controlled by spike status:

The time-frequency plots of eHFOs and non-eHFOs (detected with Union HFO detector) averaged across all patients (n=15) were plotted based on spike status (with or without spikes). Across four frequency bands, eHFOs with spikes showed higher amplitude than non-eHFOs with spikes, and eHFOs without spikes showed higher amplitude than non-eHFOs without spikes ($p < 0.0001$ in all comparisons with Welch t-test with unequal variances).

HFOs: high-frequency oscillations; eHFOs: epileptogenic HFOs

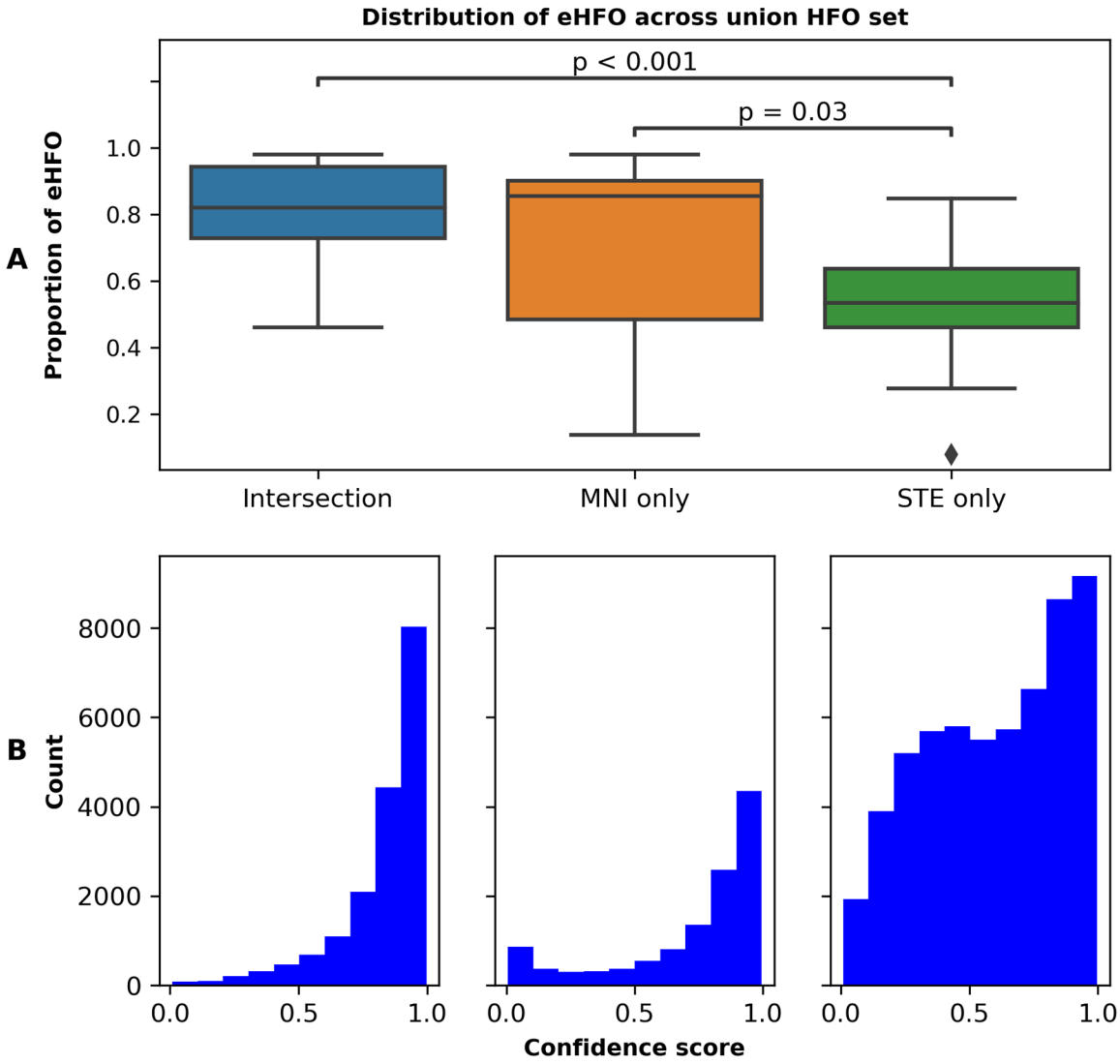

Figure 6. Distribution of eHFO in three HFO sets:

(A) Proportion of eHFO in 15 patients is plotted as box plots and labeled by the HFO set type. Across the cohort of 15 patients, MNI only set has the highest proportion of eHFO on average, followed by Intersection and STE only set. The proportion of eHFO was significantly higher in the Intersection, and MNI only set when compared to the STE only set (Intersection vs. STE only: mean 0.82 versus 0.45, $p < 0.001$; MNI only vs. STE only: mean 0.85 versus 0.45, $p = 0.03$). (B) Confidence scores of eHFOs in 15 patients were plotted as a histogram and labeled by the HFO set type. The histogram for the Intersection and MNI only set has a skewed distribution strongly biased towards 1 (direction towards eHFO), while the STE only set has a more uniform distribution.

HFOs: high-frequency oscillations; eHFOs: epileptogenic HFOs; MNI: Montreal Neurological Institute (detector); STE: Short-term energy.

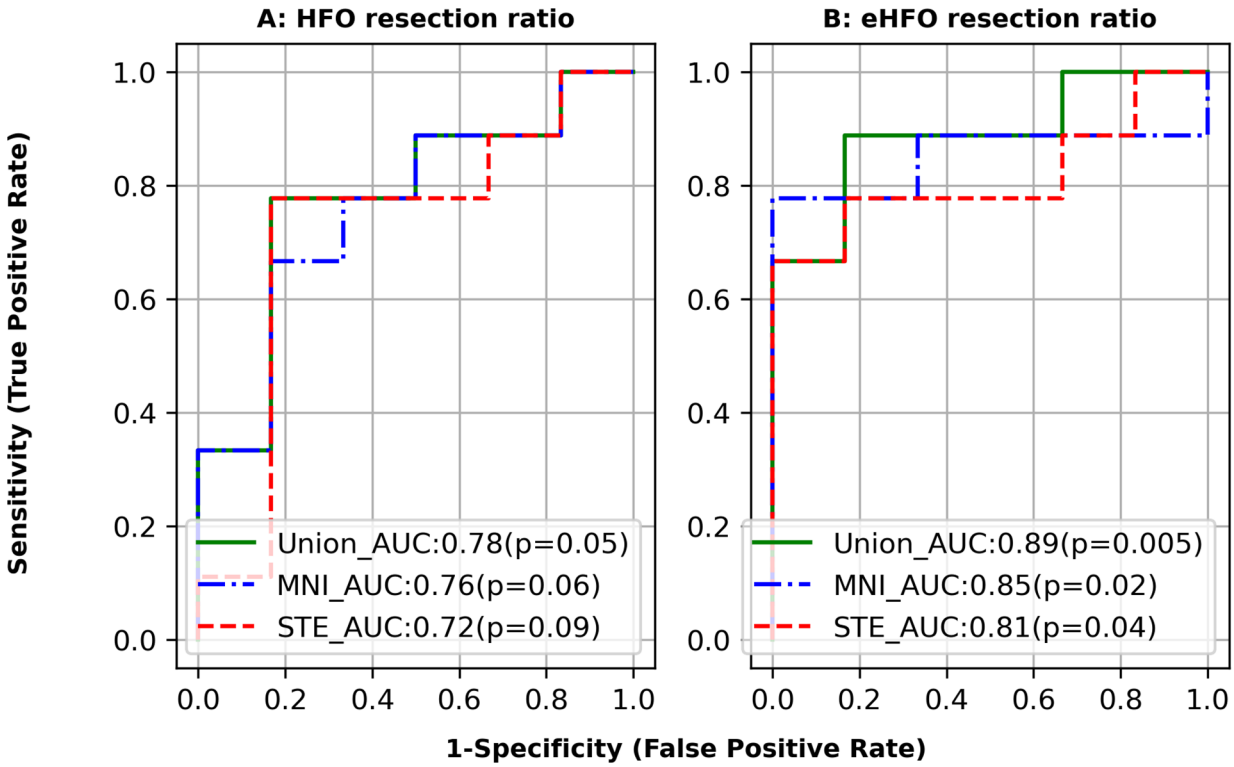

Figure 7. Accuracy of postoperative seizure outcomes using HFO resection ratios:

We constructed a postoperative seizure outcome prediction model using the resection ratio derived from 90-minute EEG data (n=15) (same approach as in our previous work (Zhang et al. 2022a). Each receiver-operating characteristics (ROC) curve delineates the accuracy of seizure outcome classification of a given model, using the area under the ROC curve (AUC) statistics. A) The HFO resection ratio (detected HFOs filtered for artifacts) obtained from 3 models (Union, MNI, and STE) was used to predict the seizure outcome. Union and MNI detectors have higher AUC values than a model obtained by the STE detector. B) eHFO resection ratio (detected HFOs filtered for artifacts and non-eHFO) obtained from 3 models (Union, MNI, and STE) was used to predict the seizure outcome. Overall significant improvement in prediction performance was seen, with the Union detector model having the highest AUC of 0.89.

HFOs: high-frequency oscillations; eHFOs: epileptogenic HFOs; MNI: Montreal Neurological Institute (detector); STE: Short-term energy.

Table 1.

hort characteristics

t No.	Sex	Age at surgery (yr)	Epilepsy duration (yr)	Anti-seizure medications	No. of ch. placed	No. of ch. resected	% of ch. resected	Duration of EEG (days)	No. of sz captured	MRI lesion/FDG-PET hypometabolism	Ch. coverage	Surgery	Pathology	No. of HFOs detected (90 min)	Inter-section HFOs	MNI only HFOs	STE only HFOs	Outcome (follow-up at 24 months)
	M	20	3	CLB, LVT, LCM	40	9	22.50%	3	21	NL/ R FP	R FP	R focal resection of sensorimotor cortex	Gliosis	959	25	10	924	Sz free
	M	11	5	CLB, CNZ, LVT, RFD, PPN	80	18	22.50%	3	26	R PO/ R PO	R FTPO	R focal resection around parietal tumor	Ganglioneurocytoma	1825	549	335	941	Sz free
	F	19	5	LVT, LCM	92	27	29.35%	5	8	R F/ R F	R FTP	R focal resection of frontal cortex	FCD 1b	11662	3760	2256	5646	Sz free
	F	14	10	CLB, LTG, LCM	64	28	43.75%	2	7	L F/ L F	L FP	L frontal lobectomy sparing sensorimotor cortex	Gliosis	5538	915	345	4278	Sz free
	M	9	1	CLB, LTG	100	83	83.00%	6	4	R TPO/ R TPO	R FTPO	R TPO	Gliosis	2488	1084	80	1324	Sz free
	F	3	2	CLB, OXC	96	42	43.75%	2	18	R F/ R FP	R FTP	R frontal lobectomy sparing sensorimotor cortex	FCD 2a	2124	78	14	2032	Not Sz free
	M	5	2	PB, PPN, OXC	104	82	78.85%	2	22	L FP/ L FP	L FTP	L frontal lobectomy including resection of sensorimotor cortex	FCD 2a	9103	904	489	7710	Sz free
	M	13	6	OXC, LTG, CLB	72	5	6.94%	6	7	R P/ R P	R FP	R focal resection of parietal cortex	FCD 2a	1894	195	701	998	Not Sz free
	F	9	7	CLB, OXC	108	43	39.81%	8	35	L F/ L FP	L FTP	L frontal lobectomy sparing sensorimotor cortex	FCD 1c	27903	3789	2676	21438	Not Sz free
0	F	8	7	LVT, LCM, CLB	66	14	21.21%	6	1	L T/ L TP	L FTP	L temporal lobectomy	Multinodular and vacuolating neuronal tumor (MVNT)	2022	291	438	1293	Sz free

t No.	Sex	Age at surgery (yr)	Epilepsy duration (yr)	Anti-seizure medications	No. of ch. placed	No. of ch. resected	% of ch. resected	Duration of EEG (days)	No. of sz captured	MRI lesion/FDG-PET hypometabolism	Ch. coverage	Surgery	Pathology	No. of HFOs detected (90 min)	Inter-section HFOs	MNI only HFOs	STE only HFOs	Outcome (follow-up at 24 months)
1	F	18	17	CLB, LTG	84	12	14.29%	3	25	L P/ L P	L FTP	L focal resection of parietal cortex	Gliosis	1409	107	31	1271	Not Sz free
2	F	15	3	LCM, LVT, OXC	86	9	10.47%	4	4	R F/ R F	R FTP	R focal resection around frontal tumor	Oligodendroglioma	1441	13	9	1419	Sz free
3	F	15	15	TPM, LTG	102	60	58.82%	4	4	L TPO/ L TPO	L FTPO	L TPO	FCD 2a, Gliosis	7914	805	1520	5589	Sz free
4	M	6	6	CLB, OXC	104	41	39.42%	11	2	L PO/ L PO	L FTPO	L parietooccipital resection	Ulegyria, FCD 3d, gliosis	19253	8254	4682	6317	Not Sz free
5	M	20	15	LCM, BVC, FBM	118	29	24.58%	12	5	L TO/ L TO	L FTPO	L temporal lobectomy plus RNS	Gliosis	2784	479	131	2174	Not Sz free

patient; M: Male; F: Female; ch: channels; sz: seizures; RNS: Responsive nerve stimulator; FCD: Focal cortical dysplasia

Left; R: Right; F: Frontal; P: Parietal; T: Temporal; O: Occipital

B: Clobazam; LVT: Levetiracetam; LCM: Lacosamide; CNZ: Clonazepam; RFD: Rufinamide; PPN: Perampanel; LTG: Lamotrigine; OXC: Oxcarbazepine; PB: Phenobarbital:

M: Topiramate; BVC: Brivaracetam; FBM: Felbamate; CLP: Clorazepate; ECZ: Eslicarbazepine.